Renewable Energy 256 (2026) 124304

Contents lists available at ScienceDirect

Renewable Energy

journal homepage: www.elsevier.com/locate/renene

CFD-based design optimization of a 5 kW ducted hydrokinetic turbine with practical constraints

Jeongbin Park [a], Marco Mangano [b], Sabet Seraj [b], Bernardo Pacini [b], Yingqian Liao [b], Bradford G. Knight [c], Kartik Naik [a], Kevin J. Maki [a], Joaquim R.R.A. Martins [b], Jing Sun [a], Yulin Pan [a,*]

[a] Naval Architecture and Marine Engineering, University of Michigan, Ann Arbor, 48109, MI, USA
[b] Aerospace Engineering, University of Michigan, Ann Arbor, 48109, MI, USA
[c] Ocean Engineering, University of Rhode Island, Narragansett, 02882, RI, USA

ARTICLE INFO

Dataset link: https://github.com/jbpark94/Ducted-Hydrokinetic-Turbine-Key-Files.git

Keywords:
Ducted hydrokinetic turbine
CFD
Gradient-based optimization
Adjoint method

ABSTRACT

Ducted hydrokinetic turbines enhance energy-harvesting efficiency by better conditioning the flow to the blades, which may yield higher power output than conventional freestream turbines for the same reference area. In this work, we present a ducted hydrokinetic turbine design obtained by simultaneously optimizing the duct, blade, and hub geometries. Our optimization framework combines a CFD solver, an adjoint solver, and a gradient-based optimizer to efficiently explore a large design space, together with a feature-based parametrization method to handle the complex geometry. Practical geometrical constraints ensure the manufacturability of the duct in terms of a minimum thickness and the housing of a 5 kW generator within the hub. The optimization converges to a short, thin duct with a rounded leading edge and an elongated hub protruding the duct inlet. The optimized ducted turbine achieves up to 50% efficiency when evaluated by RANS/URANS solvers despite a bulky hub, outperforming the 45% efficiency of the freestream Bahaj turbine featuring the same hub. This work showcases the effectiveness of CFD-based optimization in advancing ducted turbine designs and demonstrates the hydrodynamic benefits of a ducted configuration, paving the way for future research and real-world applications.

1. Introduction

Hydrokinetic turbines have gained attention over the past few decades as a promising technology for harnessing renewable energy from water currents. They offer a sustainable solution to the growing global energy demand. One key advantage of hydrokinetic energy resources is their predictable and concentrated nature, enabling continuous power generation [1]. Furthermore, hydrokinetic turbines require minimal infrastructure and have limited impact [2]. Due to these advantages, hydrokinetic turbines have been researched extensively, covering various topics such as potential site assessments [3], wake flow dynamics [4], and environmental impact analyses [5]. Horizontal-axis hydrokinetic turbines have particularly received more attention than other turbine arrangements because of their technological maturity [6].

An extensively studied topic for horizontal-axis turbines is the improvement of their energy-harvesting efficiency. One approach of growing interest is the use of a duct (also referred to as a shroud or diffuser) to condition the flow passing the turbine blades for improved efficiency [7]. Various approaches have been used to assess the performance of ducted turbines, including analytical models, experiments, and computational fluid dynamics (CFD) simulations. Analytical works, based on 1D momentum theory, have modeled different pieces of the physics, such as duct swallowing capacity [8], exit-area ratio and outlet back-pressure [9], axial force on the duct [10], and 2D effects and tip-gap [11]. Experimental works on ducted hydrokinetic turbines span a range of scales and duct geometries. For example, Scherillo et al. [12] validated two foil-shaped ducts on hydrokinetic turbines in a towing tank and wind tunnel. Shahsavarifard et al. [13] conducted experiments in a water tunnel using two simple conical duct designs, demonstrating the effectiveness of ducted hydrokinetic turbines in low-speed water flow. Nunes et al. [14] similarly demonstrated the efficiency gain through experiments in a wind tunnel using a 4-bladed turbine with lens-type and foil-type duct designs.

These analytical and experimental studies provide valuable benchmarks and insights. However, CFD simulations remain necessary to capture complex flow physics, evaluate performance reliably, and explore

* Correspondence to: Rm 208, 2600 Draper Dr. Ann Arbor, MI, 48109, USA.
E-mail address: yulinpan@umich.edu (Y. Pan).

https://doi.org/10.1016/j.renene.2025.124304
Received 20 November 2024; Received in revised form 20 August 2025; Accepted 20 August 2025
Available online 28 August 2025

alternative designs. CFD models for ducted turbines include Reynolds-averaged Navier–Stokes (RANS) and unsteady RANS (URANS). The effects of a rotor on the flow can be modeled with body-force-based methods, such as the actuator disk model. These approaches have been widely used to quantify performance gain from simple duct geometries [15], complement analytical models [16], and optimize duct shapes [17]. However, these low-order models rely on prescribed thrust distributions and do not provide insights into actual turbine power extraction. Blade element momentum theory methods [18] address this limitation by modeling sectional blade characteristics and estimating the power and thrust outputs. Further increasing the model fidelity, the full 3D geometry of turbine blades can be resolved within a computational mesh. The turbine rotation can be modeled by either multiple reference frame (MRF) [19] or rotating-sliding mesh (RS) [20]. These advancements in ducted turbine modeling enable a more accurate assessment of their performance. However, previous studies' assessments focused on single or a few turbine designs, and thus, the performance of these designs is likely far from optimal.

Developing simulation-based optimizations for ducted turbines is a considerably more challenging task, especially when the optimization is coupled with higher-fidelity simulation methods. Several RANS-based studies use gradient-free optimization methods, such as genetic algorithms [21] and simulated annealing [22]. While these efforts provided some insights into the design of ducted turbines, they only included a few design variables (up to 14) and did not necessarily achieve optimality. These shortcomings stem from the use of gradient-free optimization methods, which converge slowly and do not check for the mathematical optimality conditions [23, Ch. 7]. Additionally, the presence of strong duct–rotor interactions suggests that optimizing both components simultaneously is critical to identify a system-level optimum [20], whereas single-component or sequential approaches may lead to suboptimal solutions [23, Ch. 13]. As a result, these design efforts optimize only one component of the ducted turbine (e.g., duct only) using a small number of design variables, leaving room for further improvement.

Our previous work [24] presented the first gradient-based optimization of a ducted hydrokinetic turbine, with the gradients efficiently computed by an adjoint method coupled with a RANS solver and the MRF method [24]. This methodology enables simultaneous optimization of the blade and duct geometries (21 design variables in total), yielding an efficiency of approximately 54% when re-evaluated using a high-fidelity URANS solver coupled with the RS approach. This efficiency is significantly higher than that of the standard freestream Bahaj model, which yields 46% efficiency [25]. Despite the novel contribution, the formulation of our previous work had several limitations. First, the design excluded a hub, which is a necessary component for housing a generator for power transmission and attaching blades in actual turbines. Secondly, while several studies have proposed a foil-shaped duct cross-section (e.g., [22]), our previous duct design was restricted to a thin-walled shape due to limitations in the geometric parametrization approach.

The purpose of this work is to develop a more comprehensive design optimization of a ducted hydrokinetic turbine, overcoming previous limitations. To this end, we parametrize the ducted turbine geometry with a feature-based parametric CAD software, Engineering Sketch Pad (ESP) [26], which has been successfully used in gradient-based optimization of simpler, single-component geometries [27]. The ESP parametrization offers more direct and convenient control based on user-defined features than the previously used free-form deformation (FFD) approach [28]. These features can include coordinates, polynomial coefficients, length, radius, and sectional twist, which are then connected by cubic spline surfaces to form a smooth geometry [29]. ESP enables more precise adjustments of the global and local shape, addressing the limitations associated with the FFD method in our previous work.

We use this updated framework to perform a gradient-based optimization of a 5 kW ducted hydrokinetic turbine. A total of 37 design variables control the geometry of the blades, hub, and duct. In particular, the duct can have an arbitrary thickness profile constrained by a minimum thickness and a minimum leading edge radius of curvature. The minimum thickness is a manufacturing and structural consideration, and the minimum leading edge radius is beneficial for off-design oblique flow conditions [30]. The hub shape is allowed to change only ahead and behind a central cylindrical section that remains fixed to accommodate a generator sized from electrical considerations. In the optimization process, the efficiency of a design and its gradients are evaluated using DAFoam [31], which uses an adjoint method for gradient computation. The optimization is performed by SNOPT, which is an implementation of sequential quadratic programming [32].

The optimized design yields an efficiency of 50% (and 48%~49% after re-evaluation by a higher-fidelity URANS solver in OpenFOAM [33]) despite the bulky hub, which negatively impacts the turbine's hydrodynamic performance. This efficiency compares favorably to 32% of our baseline design of choice and 45% of a freestream Bahaj turbine with the same hub. The final design exhibits several distinct features that have not been identified before, including an elongated hub protruding from the duct inlet, a thin duct at the boundary of the constraints, and correspondingly changed blade geometry.

The paper is organized as follows. We first define and formulate the optimization problems in Section 2. In Section 3, we describe the methods used for the optimization and CFD evaluation, with a focus on the ESP parametrization and its integration into the optimization framework. The results of the optimization and CFD re-evaluations are presented and discussed in Section 4. Finally, the conclusions are provided in Section 5.

2. Problem statement

We consider a ducted hydrokinetic turbine operating in an unbounded fluid domain with uniform inflow U_∞, as shown in Fig. 1. The available inflow power to the turbine is $P_{\text{avail}} = \rho A U_\infty^3/2$, where ρ is the fluid density and A is the area of the device perpendicular to the flow. We consider A as the maximum projection area of the duct, which in this case is at the duct exit. The turbine converts the inflow power into rotational mechanical power with an efficiency characterized by the power coefficient

$$C_P = \frac{P}{P_{\text{avail}}}, \tag{1}$$

where $P = \tau\Omega$ is the mechanical power, with τ the turbine's torque and Ω its rotation speed. The conversion of the turbine shaft mechanical power into electrical power through the generator system is subject to losses as follows:

$$P_e = P \cdot \eta, \tag{2}$$

where η is the electromechanical efficiency. In this work, inflow velocity is set to $U_\infty = 1.7$ m/s, based on data of the Mississippi River [34], and $P_e = 5$ kW. The electrical components are sized based on this power and flow conditions [35]. This results in a generator with a diameter of 0.355 m and $\eta = 0.8255$. The device projection area A is estimated by considering Eqs. (1) and (2), as well as $C_P = 0.46$ according to the original Bahaj model [25]. This yields $A = 5.23$ m^2 associated with a diameter $D = 2.58$ m.

Another two relevant non-dimensional parameters are the tip-speed ratio λ and Reynolds number Re (based on the diameter of the device), defined as

$$\lambda = \frac{\Omega R}{U_\infty}, \quad Re = \frac{U_\infty D}{\nu}, \tag{3}$$

where $\nu = 10^{-6}$ m^2/s is the fluid kinematic viscosity. For the calculated D, we have $Re = 4 \times 10^6$, and thus we consider the boundary layer to

Table 1
Optimization problem statement.

	Variables/Function	Description	Quantity
Maximize	C_P	Power coefficient	1
With respect to	α	Duct cone angle	1
	A_{upper}	Duct upper polynomial coefficients	6
	A_{lower}	Duct lower polynomial coefficients	6
	β	Duct length	1
	R_b	Blade radius	1
	θ	Blade twists	9
	c	Blade chords	9
	x_{hub}	Hub control point translations	4
		Total	37
Subject to	$t_{\text{duct}} \geq 0.014$ m	Duct thickness	50
	$h = 0.05$ m	Tip gap	1
	$\rho_\kappa \geq 0.0015$ m	Duct leading edge curvature radii	1
	$A = 5.23$ m^2	Maximum area	1
	$D_{\text{hub}} = 0.4$ m	Hub cylindrical section diameter	1
	$L_{\text{hub}} = 0.78$ m	Hub cylindrical section length	1
		Total	55

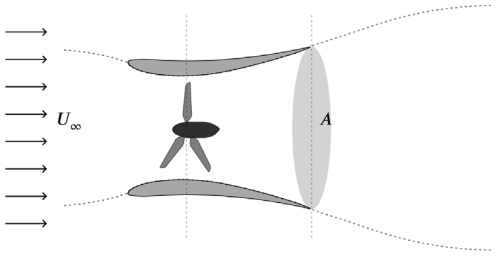

Fig. 1. The ducted turbine has a projected area A and is subject to inflow U_∞.

be fully turbulent. The performance of the turbine will be evaluated as a function of λ at this Re.

The goal of the optimization is to simultaneously optimize the geometry of blades, hub, and duct to maximize C_P at $U_\infty = 1.7$ m/s and fixed $\Omega = 8.26$ rad/s, which corresponds to the optimal λ of the baseline ducted turbine described later. The designed turbine is expected to produce a power greater than 5 kW if the optimized C_P is larger than 0.46 (the value used to calculate A). If we need P_e to be precisely 5 kW, the size of the optimized device could be adjusted to achieve this value. The complete optimization problem setup with 37 design variables is described in Table 1.

The design variables are selected to provide sufficient geometric freedom for the optimizer to explore a broad design space of the system geometry. To avoid unnecessary complexity, we limit the total number of shape and sectional variables for the duct and blade, as excessive flexibility can lead to noisy geometries without meaningful performance gains [30]. The duct design is parametrized by 14 variables that control the upper and lower surface shapes, duct cone angle, and length, as illustrated in Fig. 2(a). The upper and lower surfaces of the duct are parametrized using class-shape transformation (CST) variables [36], which are coefficients of the Bernstein basis polynomials connecting the leading and trailing edges as detailed in Appendix. The CST parametrization enables broad and flexible design exploration while maintaining a smooth foil-shaped cross-section. The variation of the CST parameters is complemented by the duct cone angle and length, which change the location of the leading edge. The duct cone angle is adjusted by pivoting around the trailing edge, with a bound on maximum rotation to ensure that no sectional area exceeds the exit area, $A = 5.23$ m^2. The duct scaling is also anchored to the trailing edge, with a scaling factor applied to all points on the duct. The above choices, with the trailing edge as the reference point, make it easier to keep the exit diameter as the maximum.

The turbine blades are parametrized by 19 variables, including the chords and twists at 9 spanwise locations and the blade radius, as illustrated in Fig. 2(b). The chords are determined by scaling factors that change the size of the section while maintaining the sectional foil shape, e.g., the thickness-to-chord ratio. Any changes to these 19 variables are equally applied to all three blades. For the turbine hub, the central cylindrical section is fixed at a diameter $D_{\text{hub}} = 0.4$ m and length $L_{\text{hub}} = 0.78$ m to accommodate the selected generator inside. To allow flexible change of hub geometry with the fixed central part, the front and rear parts are parametrized by translating 4 control points. Two points at the front and rear hub ends move axially, primarily driving the hub length. The other two points control the hub front and rear curvature by moving in the radial direction, as shown in Fig. 2(c). Once the locations of the 4 points are given, two cubic splines are used to fit the front and rear parts of the hub. We ensure slope continuity at the front end and the connection to the main hub cylindrical surface.

In addition to the constraints mentioned above on A, D_{hub}, and L_{hub}, we also impose a constraint on minimum duct thickness $t_{\text{duct}} = 0.014$ m to meet the yield strength requirements (based on a calculation using 6061 aluminum alloy). This constraint is enforced at 50 chordwise duct sections for global satisfaction. The duct leading-edge radius of curvature is constrained to a minimum of $\rho_\kappa = 0.0015$ m. This minimum leading-edge radius improves off-design performance at oblique flow conditions [30]. Finally, a constraint on a constant tip gap of $h = 0.05$ m is set between the duct and blade surfaces. In the optimization, the constraint values A, t_{duct}, ρ_κ, and h can all be computed as direct or indirect functions of the design variables (see Appendix, particularly for ρ_κ) and can therefore be treated as standard equality or inequality constraints.

In this work, the baseline blade geometry is taken from the optimized design A in our previous work [24], with NACA 63-8xx sectional shapes and a blade radius of 1 m. The baseline hub geometry consists of a hemisphere for the front part and a half ellipsoid of length 0.527 m for the rear part. The baseline duct uses an Eppler 423 (E423) foil shape, which is known for its high lift coefficient [37], scaled for a chord length of 3.013 m and maximum thickness of 0.129 m and then rotated to maintain the tip gap of $h = 0.05$ m — see Figs. 10 and 11 in Section 4.1.

3. Method

Our overall methodology is summarized in Fig. 3, which shows two major components intertwined with each other: gradient-based optimization and CFD simulations. The key procedure is described as follows.

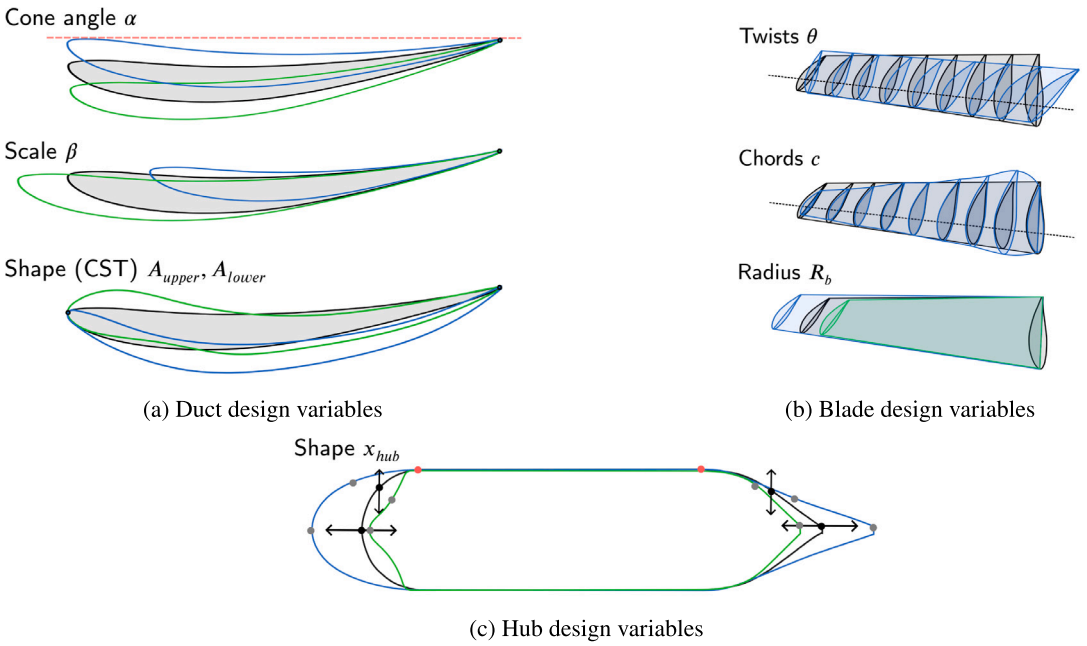

(a) Duct design variables

(b) Blade design variables

(c) Hub design variables

Fig. 2. Design variables for (a) duct, (b) blade, and (c) hub. The baseline design is shown in black, with blue and green illustrating two examples of deformed configurations.

1. The baseline geometry is parametrized with Engineering Sketch Pad (ESP) method implemented in the pyGeo package [28]. A computational mesh is generated using Pointwise.[1]
2. DAFoam's RANS solver *DASimpleFoam* [31] with multiple reference frames (MRF) and Spalart–Allmaras (SA) turbulence model [38] evaluates the performance of the ducted turbine and predicts a C_P.
3. The gradient $dC_P/d\boldsymbol{x}$ is computed using the discrete adjoint method, where $\boldsymbol{x} \in \mathbb{R}^{37}$ is the vector of design variables. The discrete adjoint method is an approach for efficient derivative computation, with the computational cost independent of the dimension of $\boldsymbol{x}$. This solver is also implemented in DAFoam.
4. The next design point is identified through a sequential quadratic programming algorithm implemented in SNOPT [32], using information from Steps 2 and 3, as well as the specified constraints.
5. The computational mesh is deformed according to the new set of design variables $\boldsymbol{x}$ in two steps. First, the surface mesh is updated based on the updated ESP geometry. Then, the surface deformation is propagated to the volume mesh through the analytic inverse-distance weighting method [39] implemented in the IDWarp package [40].
6. Steps 2 to 5 are repeated until the optimality convergence criteria are met, after which the optimized design is obtained.
7. After the steady RANS-based optimization, URANS solver *pimpleFoam* with a rotating-sliding mesh (RS) in OpenFOAM [33] and $k-\omega$ shear stress transport (SST) turbulence model [41] re-evaluates the performance of the optimized design on a mesh generated using *snappyHexMesh*.

Most components involved in the above procedure are detailed in our previous work [24], except for the ESP parametrization and its integration into the mesh generation and deformation within the optimization process. In the following sections, we provide detailed descriptions of the ESP parametrization and the associated mesh generation using Pointwise, followed by the mesh generated with *snappyHexMesh* for URANS re-evaluation in Step 7. The key files for this work are publicly available.[2]

3.1. ESP and pointwise mesh

Our previous optimization work [24] had two major limitations: the exclusion of a hub and the restriction of a duct to a thin-walled cross-section, as discussed in Section 1. These limitations were related to the FFD approach [28] that we used for the geometry parametrization. In particular, it is challenging to separately control the deformation of the hub and blades through FFD, as they are attached and have to be controlled by the same FFD box enclosing the geometry. Moreover, when FFD manipulation is applied to a foil-shaped duct, the deformation inevitably breaks the circular and axisymmetric shape. These limitations become particularly problematic as multiple tightly spaced components require independent and precise control. To overcome these limitations, we use ESP [26] in this work.

The entire ducted turbine geometry is generated and parametrized using ESP, with the design variables listed in Table 1 and illustrated in Fig. 4. ESP generates the blade surface by blending sectional NACA 63-8xx shapes at nine spanwise locations with desired twists θ and sectional chords c using cubic spline surfaces. For the hub, cubic splines are generated using four control points to shape the front and rear sections, ensuring slope continuity at the hub's front end and junctions with the central cylindrical section of the hub. The curves are then revolved around the hub's longitudinal axis to form the full axisymmetric hub surface. The duct foil shape is defined by the CST variables A_{upper} and A_{lower} scaled by a factor β and rotated by an angle α with respect to the trailing edge, which is then revolved around the axial axis to create the complete duct geometry.

We use Pointwise to generate high-quality surface and volume meshes. Based on the geometry information provided by ESP, we discretize the surfaces using triangular elements for the blade and hub surfaces and quadrilateral elements for the duct surface. The volume mesh, mainly composed of tetrahedral elements, is then generated to

[1] Cadence Fidelity Pointwise for CFD Meshing https://www.cadence.com/en_US/home/tools/system-analysis/computational-fluid-dynamics/fidelity.html#fidelity-pointwise.

[2] https://github.com/jbpark94/Ducted-Hydrokinetic-Turbine-Key-Files.git.

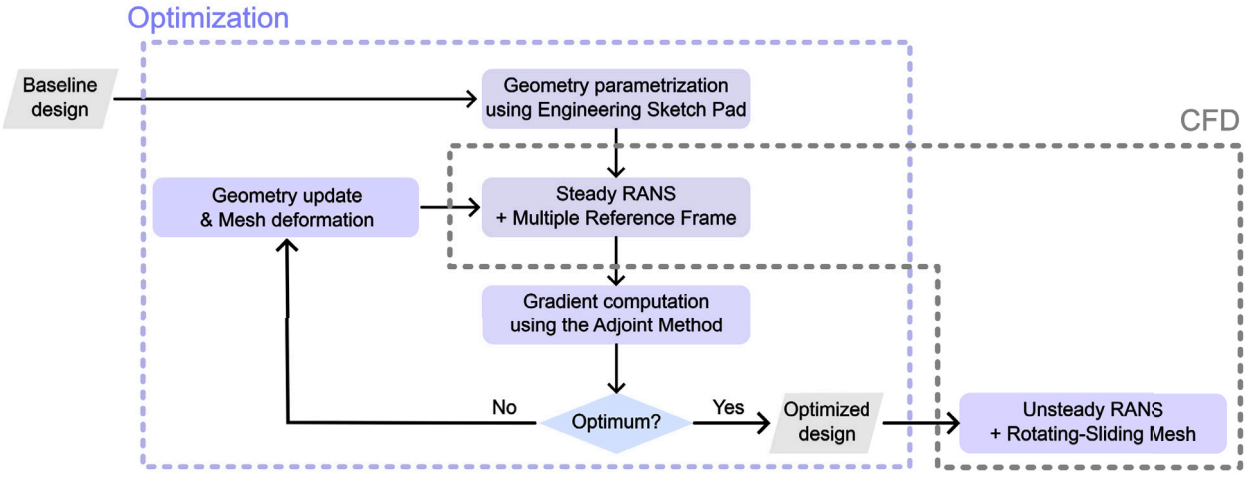

Fig. 3. Flowchart of the optimization and CFD simulation processes.

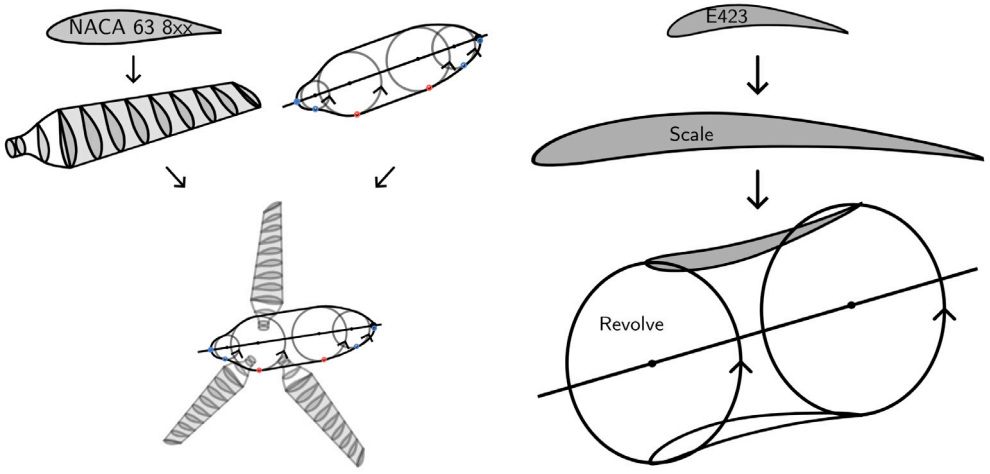

(a) ESP model of the turbine. (b) ESP model of the duct.

Fig. 4. ESP model of the ducted turbine. (a) The turbine geometry is created by combining three blades and a hub. The blades are generated by blending NACA 63-8xx hydrofoils along the span, with rotation and scaling applied according to the desired twist and chord distributions. The hub shape is generated by spline curves based on four control points, ensuring slope continuity at the hub's front end and the junctions with the central cylindrical section and revolving the curves around the hub's axial axis. (b) The duct cross-section is defined using 12 CST variables, a conning angle, and a scale factor. The cross-section revolves around the axis to create the 3D duct geometry.

fill the space between the body surface and the domain boundary. Our computational mesh has a total of 6.3 million cells and is shown in Fig. 5. The domain size is chosen based on preliminary tests, resulting in a blockage ratio of less than 1% such that boundary effects are negligible [42,43]. Meshing with Pointwise allows a precise representation of the body surfaces, which is difficult to achieve with other automated methods such as *snappyHexMesh*, used in our previous work [24]. Inaccurate surface representations are usually more problematic at corners such as the trailing edges of the blades, which can lead to poor optimization convergence, among other issues.

The mesh deformation in Step 5 also requires ESP integration. To understand this, let us first express the mapping from the ESP surface to the mesh nodes as a function f_S. In particular, for an ESP-generated cubic spline surface S, the location of any mesh node on it is written as

$$\boldsymbol{X}_i = f_S(\boldsymbol{x}, u_i, v_i), \tag{4}$$

where $u_i \in [0,1]$ and $v_i \in [0,1]$ are normalized local coordinates of the surface S, $\boldsymbol{X}_i$ is the nodal location in global coordinate with i looping over all nodes on surface S. In a surface mesh, the locations of u_i and v_i are stored for all nodal locations. When the design variable $\boldsymbol{x}$ is updated, the new location of $\boldsymbol{X}_i$ is computed with u_i, v_i, and the function f_S remaining the same [44]. The volume mesh is then updated using the analytic inverse-distance weighting method [40].

3.2. *snappyHexMesh for URANS simulations*

We switch to *snappyHexMesh* for the higher-fidelity URANS-RS re-evaluations in Step 7. While the Pointwise mesh provides the exact representation of the body surfaces, it usually includes highly non-orthogonal cells. These cells prohibit efficient URANS simulations because additional correction steps are needed at each iteration, and the whole process is costly in our current setting. The mesh generated using *snappyHexMesh* is predominantly composed of hexahedral cells with

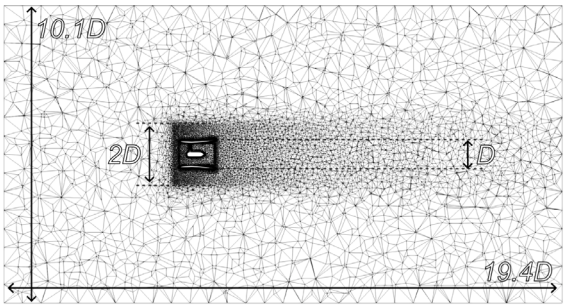

(a) Side view

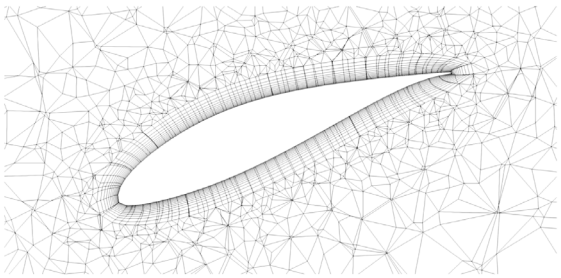

(b) Close-up of the $0.5R$ blade section

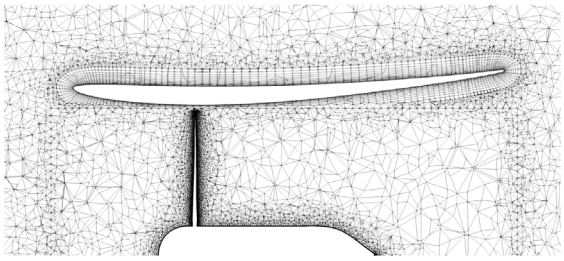

(c) Close-up near the duct and hub

Fig. 5. The mesh generated by using Pointwise predominantly composed of tetrahedral cells. The domain of the mesh is $10.1D \times 10.1D \times 19.4D$. The mesh is refined around the ducted turbine geometry, and the near-surface regions are further refined using 15 prism layers with an expansion ratio 1.2 and an initial cell spacing of 0.001 m for the duct and 5×10^{-5} m for the blade and hub, resulting in a total cell count of 6.3 million.

a domain of size $12.3D \times 12.3D \times 20.9D$, as shown in Fig. 6. In a region of $3D \times 3D \times 8.2D$ surrounding the turbine, each cell undergoes a level-4 refinement, subdividing each initial cell into 2^4 cells per direction. Further refinements of levels 6 and 9 are applied towards the duct, blade, and hub surfaces, respectively. Three prism layers with an expansion ratio of 1.2 are added near the turbine and duct surfaces to improve the near-wall resolution. The near-wall refinement is designed to achieve a y^+ of around 30, within the range where OpenFOAM's automatic wall treatment [45] has been demonstrated to perform robustly. We use these strategies to generate meshes with different cell counts by varying the resolution of the base mesh. Ducted turbine performance will be evaluated on these different meshes.

4. Results and discussion

Before presenting the optimization results, we first present the RANS and URANS analysis for a 5 kW freestream Bahaj turbine featuring the baseline hub, compared to the experimental data at a smaller model scale [25]. Fig. 7 plots the power coefficient C_P and thrust coefficient $C_T = T/(0.5\rho U_\infty^2 A)$ for various mesh resolutions. For the RANS simulations, we consider the results converged when the residual of the momentum equation decreases below $\mathcal{O}(10^{-6})$. For the URANS simulations, we consider the simulation to be converged if the change in mean C_P between small time windows (~0.025 s) is less than 10^{-6}. The final C_P is then calculated by averaging over the remaining simulation time. Both the RANS-MRF and URANS-RS results converge well with mesh refinement and compare reasonably with the experimental data. When interpreting the difference between simulation and experimental results, we need to keep in mind that the simulations are performed for a much larger turbine (of blade radius 1.29 m, approximately three times larger than the experiments) and a hub with a much larger relative size (the exact size not specified for experiments in the paper).

Next, we evaluate the power coefficient C_P of the baseline ducted turbine design as a function of tip speed ratio λ using the RANS-MRF approach. As shown in Fig. 8, the peak $C_P = 0.321$ is obtained at $\lambda = 4.86$ (corresponding to a turbine rotation rate of $\Omega = 8.26$ rad/s) among 6 values of λ ranging from 3.86 to 6.36. At $\lambda = 4.86$, we re-evaluate the performance using the URANS-RS method, which provides a similar value of C_P. The optimization problem described in Table 1 is then performed at $\lambda = 4.86$.

4.1. Optimization

We solve the optimization problem described in Section 2 following the procedure outlined in Section 3. Fig. 9 shows the evolution of the power coefficient C_P throughout the optimization process. Starting from the baseline design with $C_P = 0.301$, the optimization achieves a final design with $C_P = 0.501$ after 291 iterations. This took 17 days and 2 h of wall time using 512 cores in Intel Xeon 8352Y processors on the TAMU FASTER cluster. The initial C_P differs from the value 0.321 shown in Fig. 8 because of the coarser mesh, the SA turbulence model, and a lower-order numerical scheme in optimization for stable adjoint solver convergence. This is similar to what we found in our previous work [24]. The red crosses on the graph indicate points where re-meshing is necessary due to excessive mesh distortion that triggers IDWarp failures.

The optimization is considered complete when C_P plateaus, despite further mesh adjustments. While this approach is not numerically rigorous, it is appropriate for practical engineering design considerations. The SNOPT optimality metric [32] decreases from 10^{-1} to $10^{-2.28}$, which is a reduction of more than one order of magnitude. Numerical noise on the function derivatives and the re-meshing process prevents a lower optimality value. When C_P remains unchanged with additional re-meshing, we treat this as the optimal point where further C_P gains would likely be overshadowed by numerical noise.

Fig. 10 compares the optimized geometries of the hub and duct to the baseline, and Fig. 11 makes the same comparison for the blades. The duct section evolves from a thick foil shape to a thin, highly cambered profile with a slightly rounded leading edge. The leading edge curvature constraint of $\rho_\kappa = 0.0015$ m is active. The thickness constraint of $t_{\text{duct}} = 0.0014$ m is also active away from the leading edge, with a smooth transition to thinner airfoil sections enabled by the ESP parametrization. The optimization favors a thin-walled duct over a duct with larger thickness because for fixed outlet area A, a

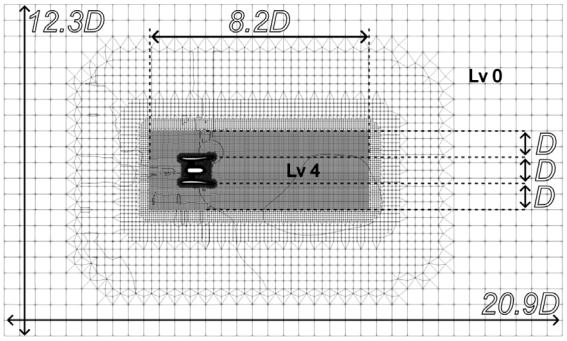

(a) Side view

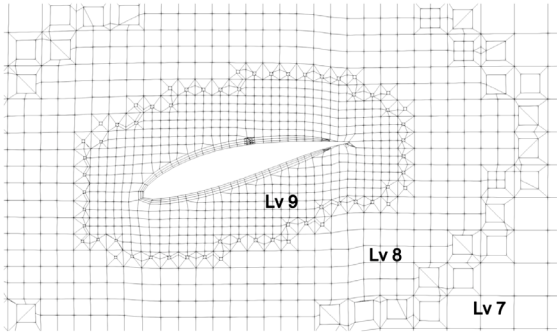

(b) Close-up of the blade section at $0.5R$

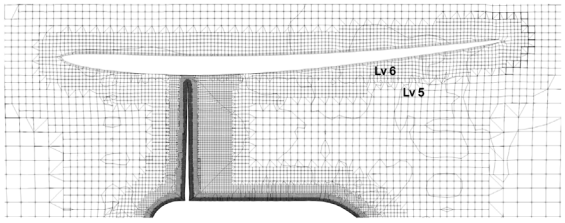

(c) Close-up near the duct and hub

Fig. 6. The mesh generated using *snappyHexMesh* predominantly contains hexahedral cells. The domain of the mesh is $12.3D \times 12.3D \times 20.9D$. We add a refinement region around the ducted turbine with a size of $3D \times 3D \times 8.2D$, with prism layers that further resolve the near-wall region.

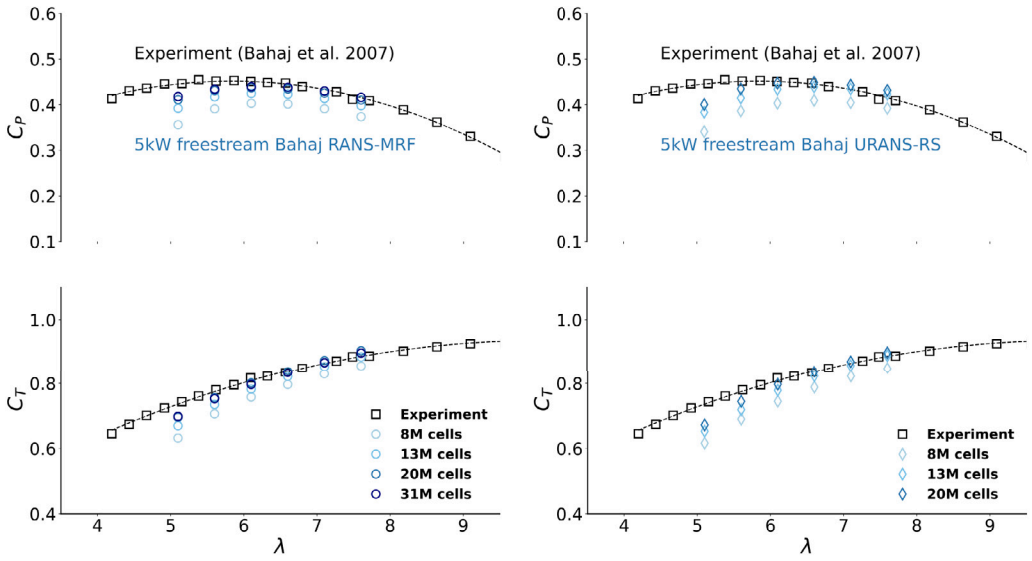

Fig. 7. Comparison between RANS (left column) and URANS solvers (right column) with varying mesh resolutions against experimental results for the Bahaj turbine [25].

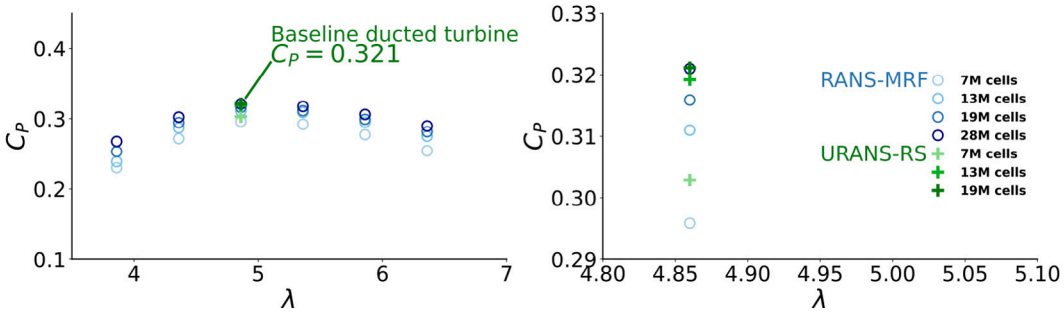

Fig. 8. Power coefficient C_P of the baseline ducted turbine as a function of λ evaluated using RANS-MRF (∘) and URANS-RS (+) with varying mesh resolutions. The right panel provides a close-up view of the results at $\lambda = 4.86$.

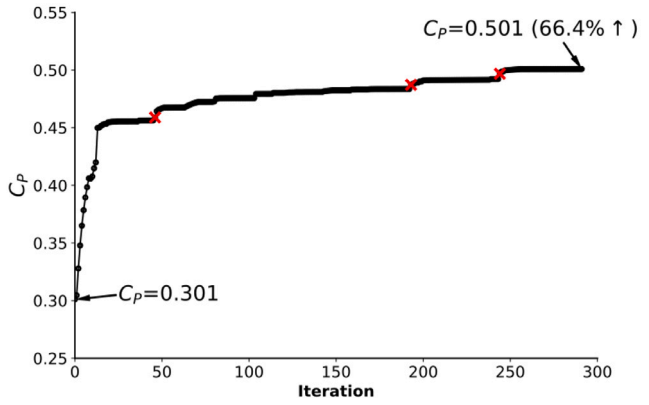

Fig. 9. Power coefficient C_P versus iteration during the optimization process. Red crosses indicate the points where re-meshing becomes necessary due to significant mesh distortion.

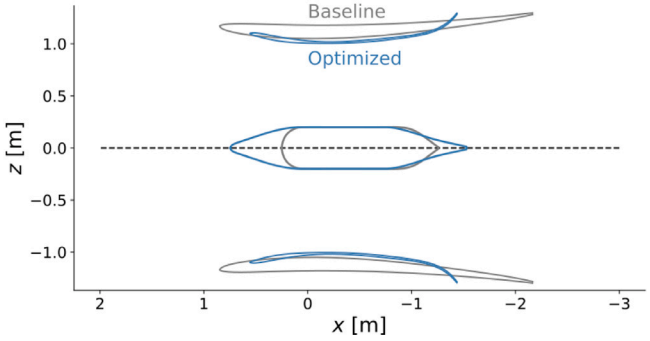

Fig. 10. Comparison of the optimized duct and hub with the baseline design.

thin-walled structure allows for a more cambered profile and a larger blade radius R_b (in our case, R_b decreases only slightly from 1 m to 0.958 m). Physically, a higher camber and higher cone angle α (also observed in the optimized design) generate a stronger circulation in the duct. This increases flow acceleration through the duct and, ultimately, a higher flow rate across the turbine blades, which increases turbine performance. The relation between performance and flow rate is discussed in our previous work [24]. The optimized design shows a tradeoff between the flow acceleration and reduced blade radius, both direct consequences of the higher camber on a fixed-outlet-area configuration.

The optimized hub features an elongated shape, with its front end protruding in front of the duct inlet. This configuration moves the stagnation point at the hub front further upstream, allowing more streamwise distance for flow acceleration before reaching the turbine blades. For the turbine blades, the optimized design exhibits substantially increased chords, particularly between $0.4R$ and $0.8R$, where the majority of power is extracted. The section twist angles increase over the span, with more significant changes occurring near the hub to accommodate the bulky hub's influence. Such a large deformation is due to the baseline blade design not considering hub effects [24].

Finally, the section closest to the hub (left-most points in Fig. 11(a)) shows a small deviation from the baseline, likely as a result of our procedure to limit mesh deformations at the blade–hub connection. These deformations can negatively affect convergence in the RANS and discrete adjoint solvers. To mitigate this issue, we add tight bounds on the variation of this section for each optimization iteration, which leads to smaller changes in the twist and chord of the first blade section closest to the hub and a rather abrupt transition to the second section. These constraints are gradually relaxed with each optimization restart and are ultimately not active in the final design. Nevertheless, this approach may limit design space exploration in exchange for optimization robustness. Future work with more robust meshing deformation algorithms could explore and leverage larger chord and twist changes, potentially further improving the ducted turbine's performance.

Table 2
URANS-RS re-evaluation results of the optimized design with different mesh resolutions, including cell counts, C_P, C_T, as well as average y^+ values on both duct and blades. These y^+ values are within the acceptable range for the automatic wall treatment used in our study.

Cells	y^+ Blade	y^+ Duct	C_P	$C_{T,blade}$	$C_{T,duct}$
4.4M	45.0	118.9	0.450	0.428	0.474
7.9M	34.2	74.8	0.485	0.446	0.503
13.4M	27.0	55.4	0.490	0.451	0.508
19.7M	22.3	46.2	0.480	0.443	0.487

4.2. Re-evaluation

4.2.1. Performance metrics

In this section, we re-evaluate the performance of the optimized design using a higher-fidelity URANS-RS method as discussed in Section 3. These URANS simulations for ducted turbines are more computationally expensive than those for freestream turbines because ducted turbines take a longer time to reach a stationary state of performance. With the same convergence criterion as for the freestream turbines (see Section 4), a typical simulation on a mesh of 13.4M cells requires at least 18 s of simulated physical time, equivalent to approximately 24 turbine rotations. With an adaptive time step averaging 10^{-4} s (rotating 0.04° per time step), the simulation takes approximately 10 days and 20 h of wall time using 256 cores on the same cluster.

Fig. 12 presents the time series of C_P from the simulation, showing the convergence of its value at the end of the simulation. Table 2 summarizes the URANS results. The results include C_P, C_T, as well as average y^+ values on both duct and blades obtained using four meshes with different cell counts. The y^+ values are within the range where OpenFOAM's automatic wall treatment has been demonstrated to perform robustly [45]. When increasing the number of cells, the value of C_P converges to a range between 0.48 and 0.49, consistent with the RANS simulation despite exhibiting oscillatory behavior. Considering both RANS and URANS results, a value of C_P up to 50% is expected for the optimized design. This value of C_P is considerably higher than the maximum that can be achieved by the freestream turbine over a range of λ. The freestream turbine with the bulky baseline hub achieved a C_P of about 45% according to the RANS and URANS results shown in Fig. 7. The optimization of the freestream turbine does not provide a significant performance improvement [24], but adding a duct improves the turbine performance even when the hub is present. Moreover, the overall C_T value for the entire ducted turbine is between 0.92 and 0.96, as shown in Table 2. This is higher than for the freestream turbine's $C_T = 0.838$ (see Fig. 7). The higher C_T value indicates an increased total force on the system. However, the C_T on the rotor itself is substantially reduced in the ducted turbine. This may be advantageous when anchoring the device on-site because it lowers the force directly acting on the rotor and shifts more of the load onto the surrounding structure.

The value of C_P from the RANS simulations of the current design (0.501) is higher than that of the design from our previous work [24] (0.482). However, the URANS results show a different trend, with $C_P = 0.48\sim0.49$ and $0.54\sim0.55$ for the current and previous designs, respectively. The uncertainty in CFD simulations due to mesh and modeling errors must be taken into account when comparing these two cases.

Besides this uncertainty, two factors in the current design could negatively affect the performance in terms of C_P. The first factor is

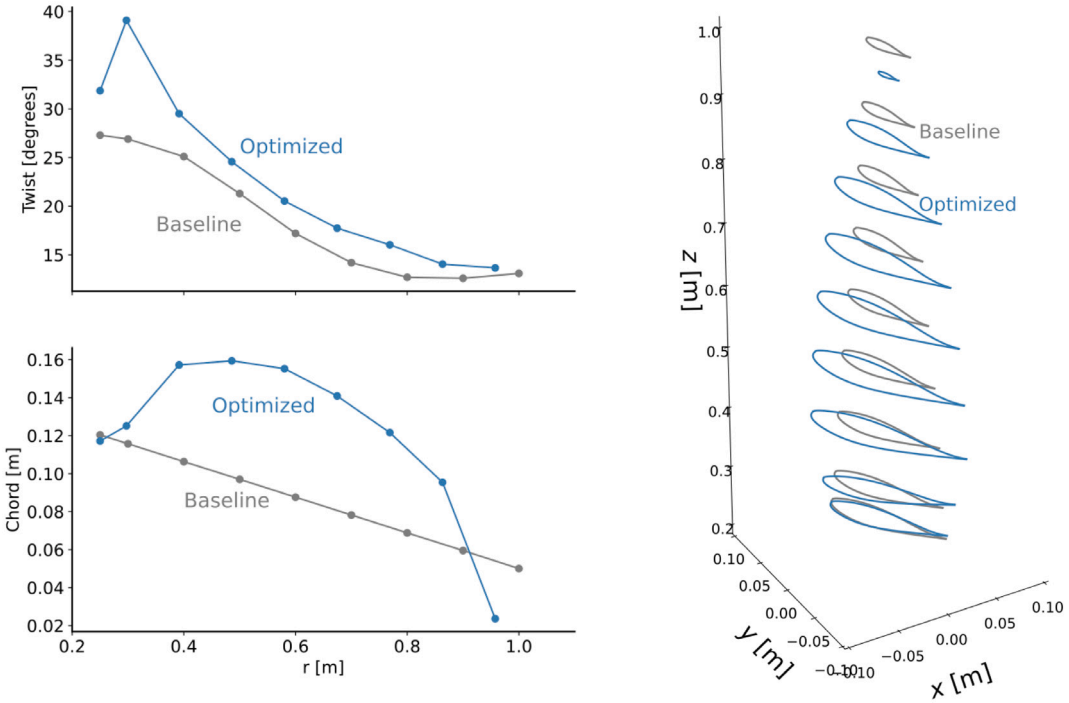

(a) Twist and chord profiles (b) Spanwise sections

Fig. 11. Comparison of the optimized blade with the baseline design.

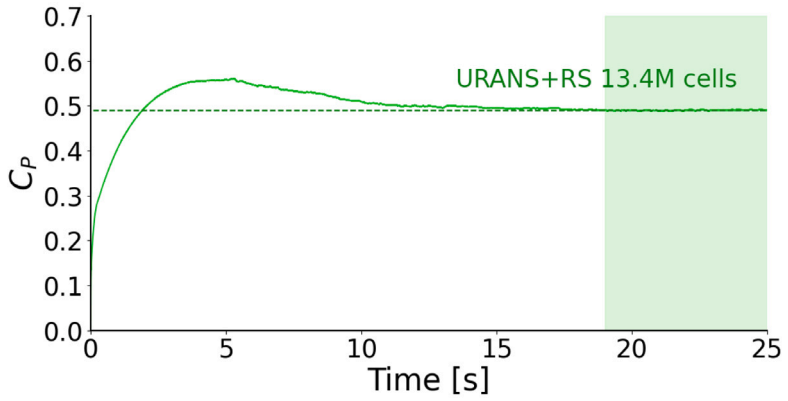

Fig. 12. Power coefficient C_P as a function of time from the URANS-RS simulation on the mesh with 13.4 million cells. Convergence is declared once the change in mean C_P between small time windows (~0.025 s) is less than 10^{-6}. The final C_P is then calculated by averaging over the remaining simulation time (shaded area).

the bulky hub, which tends to reduce the flow velocity and occupy the space that could otherwise be used by the blades for power extraction. The second factor is the bound on the leading edge radius of curvature. The rounded leading edge tends to improve the performance at off-design conditions (e.g., oblique inflow) with some sacrifice of the performance at the on-design condition [30]. Considering the additional constraints and hub negatively affecting the peak performance, the current design's performance exhibiting considerably higher C_P compared to the unducted counterpart should be applauded. This achievement showcases once more the hydrodynamic benefits of ducted turbine configuration.

Fig. 13 plots the values of C_P obtained with the URANS solver using the 13.4M cell mesh for λ from 3.70 to 6.09, where the shift in λ reflects the reduced blade radius after optimization. The optimized ducted turbine achieves a higher maximum C_P of approximately 0.49, compared to 0.32 for the baseline and 0.44 for the unducted counterpart, with all C_P values obtained using meshes of comparable resolution. Despite being optimized at a fixed Ω = 8.26 rad/s, it maintains high performance across a wide range of λ, demonstrating robustness under varying operating conditions. This further supports the advantage of the optimized ducted turbine in realistic situations with a time-varying tip speed ratio.

4.2.2. *Flow field features*

We finally compare some key flow features between the optimized and baseline designs. Fig. 14 shows the iso-surfaces of the Q-criterion, which is defined as difference between local rotational and strain rates, commonly used to visualize vortex structures (see detailed mathematical definition in the caption of the figure) [46]. For both designs, we observe helical tip and root vortices, along with ring-shaped vortices formed near the duct trailing edge. For the optimized design, the short

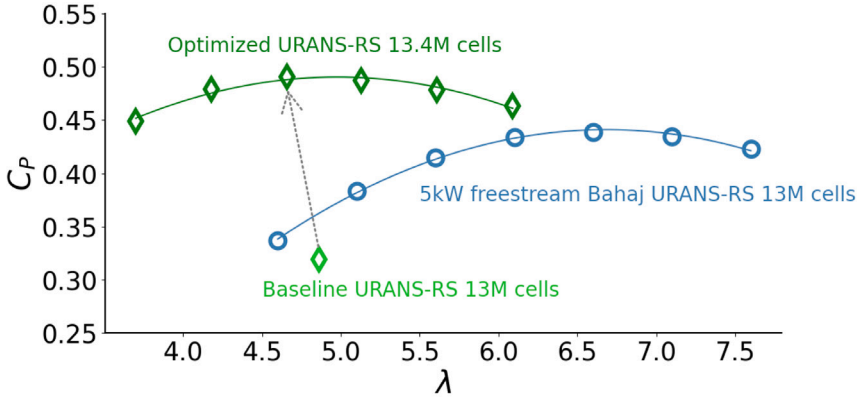

Fig. 13. Comparison of power coefficient C_P between the optimized ducted turbine and the 5 kW freestream Bahaj with the baseline hub over a range of λ, using a mesh with a similar number of cells. The dotted arrow indicates the performance improvement achieved through optimization.

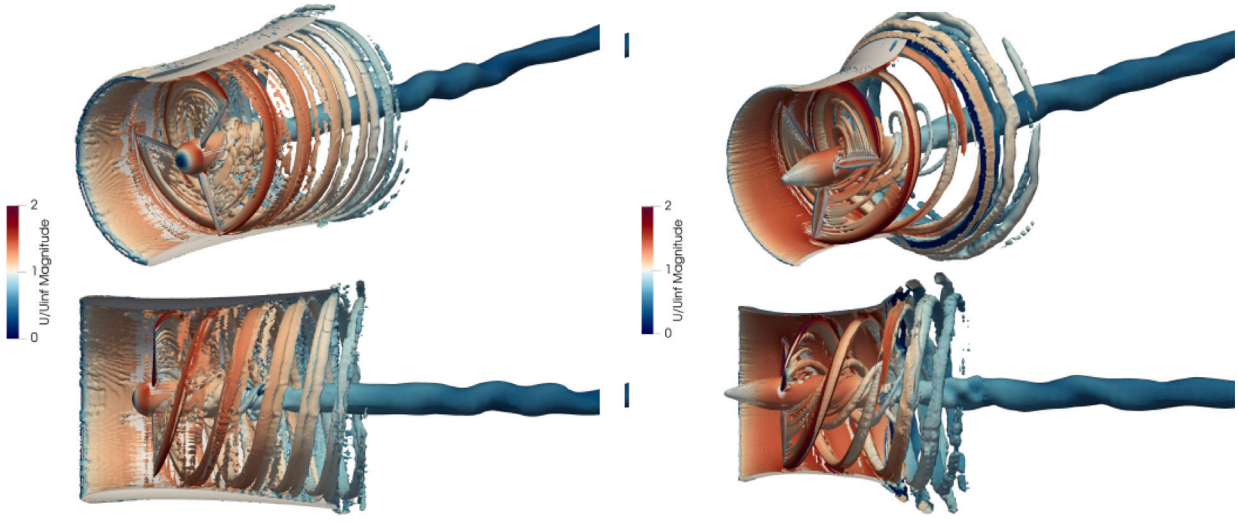

Fig. 14. Iso-surfaces of Q-criterion = 1 of the baseline design (left) and the optimized design (right) colored by the magnitude of normalized velocity ($\mathbf{U}/U_\infty$). Q-criterion is defined as $Q = (\|\mathbf{R}\|^2 - \|\mathbf{S}\|^2)/2$, where $\mathbf{R} = (\nabla\mathbf{U} - (\nabla\mathbf{U})^T)/2$ and $\mathbf{S} = (\nabla\mathbf{U} + (\nabla\mathbf{U})^T)/2$ are rotation tensor and strain rate tensor, respectively.

and highly cambered duct drives a faster radial expansion of the flow, which is visualized as an expanding helical tip vortex with a tighter axial spacing downstream of the duct. Additionally, the optimized case shows earlier decay of the vortices compared to the baseline, consistent with the literature [47].

Fig. 15 and 16 present the in-plane velocity vectors and the contours of pressure coefficient, respectively, for the baseline and optimized ducted turbines. The highly cambered duct profile of the optimized design generates stronger axial acceleration through the throat and a more pronounced outward flow deflection towards the exit. The c_p contours show the corresponding broader lower-pressure region both inside the duct and immediately downstream. These features are consistent with a higher flow rate through the turbine, leading to increased efficiency. Additionally, the elongated hub shifts the flow stagnation point (and its corresponding high-pressure region) farther upstream of the duct inlet. The longer distance between the hub nose and the blades allows more room for flow to accelerate and further contributes to the performance improvement.

5. Conclusions

In this study, we conduct a gradient-based design optimization of a 5 kW ducted hydrokinetic turbine using CFD and the adjoint method. We optimize a total of 37 design variables, parametrizing the duct, blade, and hub geometries. We built this parametrization with ESP and used it to construct practical geometric constraints, including a minimum hub size to house the generator and a minimum duct thickness for manufacturing and structural considerations.

Our optimized design yields significantly improved performance relative to the baseline design at a broad range of λ, achieving a C_P of up to 50%. The optimized design's features include a hub protruding from the inlet of the duct, a highly cambered thin-walled duct constrained only by the thickness and leading edge curvature constraints, and blades with increased twist near the base and enlarged chords in their midspan. All these features have different physically beneficial effects on the turbine's performance.

This work demonstrates the effectiveness of using gradient-based optimization with practical geometry constraints in the design of high-efficiency ducted hydrokinetic turbines. In future work, the optimization problem could be extended to include supporting structures for the hub, either as constraints or additional design variables. Such continued efforts aim to push the boundaries of performance in ducted turbine systems and enhance their viability for renewable energy applications.

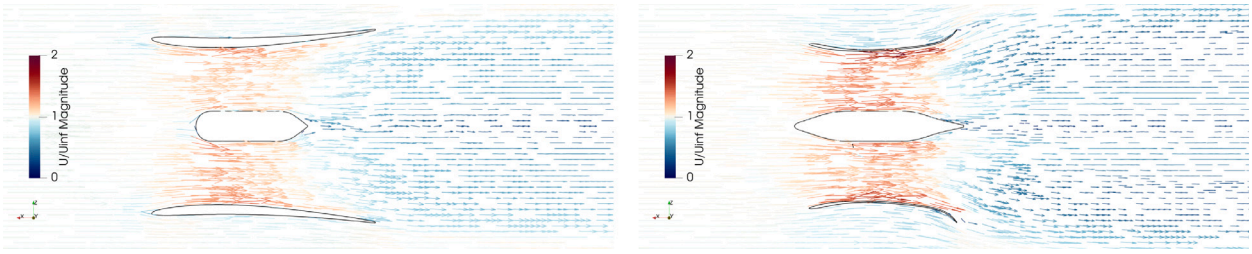

Fig. 15. Velocity vectors of the baseline design (left) and the optimized design (right) colored by the magnitude of normalized velocity ($\mathbf{U}/U_\infty$).

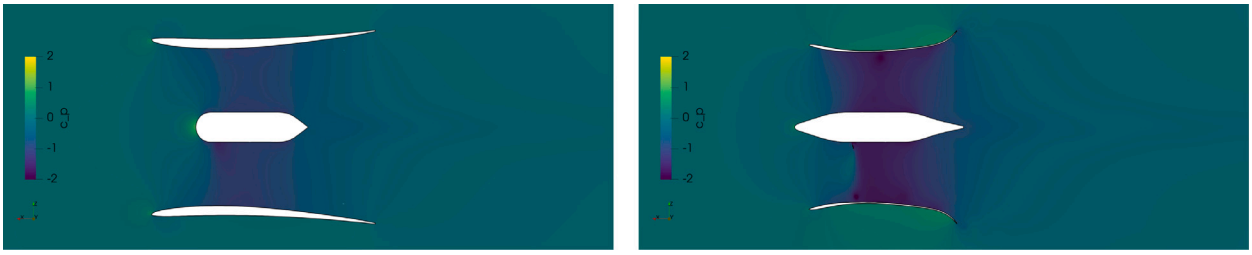

Fig. 16. Pressure coefficient, $c_p = (p - p_\infty)/(0.5\rho U_\infty^2)$, of the baseline design (left) and the optimized design (right).

CRediT authorship contribution statement

Jeongbin Park: Writing – review & editing, Writing – original draft, Visualization, Validation, Methodology, Investigation, Formal analysis, Data curation, Conceptualization. **Marco Mangano:** Writing – review & editing, Software, Methodology, Investigation, Formal analysis, Conceptualization. **Sabet Seraj:** Writing – review & editing, Software, Methodology, Investigation, Formal analysis. **Bernardo Pacini:** Writing – review & editing, Software, Methodology, Investigation, Formal analysis. **Yingqian Liao:** Writing – review & editing, Software, Methodology. **Bradford G. Knight:** Writing – review & editing, Methodology. **Kartik Naik:** Writing – review & editing, Project administration. **Kevin J. Maki:** Writing – review & editing, Supervision, Methodology, Investigation, Funding acquisition, Formal analysis, Conceptualization. **Joaquim R.R.A. Martins:** Writing – review & editing, Supervision, Software, Methodology, Investigation, Funding acquisition, Formal analysis, Conceptualization. **Jing Sun:** Writing – review & editing, Supervision, Resources, Project administration, Investigation, Funding acquisition, Formal analysis, Conceptualization. **Yulin Pan:** Writing – review & editing, Writing – original draft, Supervision, Resources, Project administration, Methodology, Investigation, Funding acquisition, Formal analysis, Conceptualization.

Declaration of competing interest

The authors declare that they have no known competing financial interests or personal relationships that could have appeared to influence the work reported in this paper.

Acknowledgments

This work was supported by the US Department of Energy under the award "RAFT: Reconfigurable Array of High-Efficiency Ducted Turbines for Hydrokinetic Energy Harvesting" (Award No. DE-AR0001438). The authors thank DOE ARPA-E Submarine Hydrokinetic And Riverine Kilomegawatt Systems (SHARKS) Program led by Mario Garcia-Sanz. We also thank the entire RAFT Team, especially Onur Bilgen, Gregory Methon, and Nazim Erol from the Structural team, Yue Cao, Md Tariquzzaman and Peidong Li from the Electrical team, and Ruo-Qian (Roger) Wang and Eshwanth Asok from the Environmental team, for their valuable discussions during the work. Help from Ping He on DAFoam is also greatly appreciated. This work utilized the FASTER high-performance computing cluster at Texas A&M University through allocation PHY220115. This computing allocation is supported by the Advanced Cyberinfrastructure Coordination Ecosystem: Services & Support (ACCESS) program, which is funded by National Science Foundation, United States grants #2138259, #2138286, #2138307, #2137603 and #2138296.

Appendix. Foil shape parametrization using Class-Shape Transformation (CST)

The class-shape transformation (CST) [36] parametrization provides a flexible and efficient representation of complex geometries, such as foils in our case, through the multiplication of class and shape functions. The class function C defines the overall shape category or "class" of geometry, given in generic form by:

$$C(\psi) \equiv \psi^{N_1}(1-\psi)^{N_2}, \tag{5}$$

where the coordinate ψ varies from 0 to 1, and the exponents N_1 and N_2 define the type of geometry. In the case of foil shape, $N_1 = 0.5$ and $N_2 = 1$ are typically used to create a round leading edge and a pointed trailing edge.

The detailed geometry is further refined by multiplying a shape function on the class function. A family of well-behaved analytical functions is commonly chosen to generate the shape function S, for example, the Bernstein basis polynomials used in our case:

$$S(\psi) = \sum_{i=0}^{n} A_i \cdot \binom{n}{i} \psi^i (1-\psi)^{n-i}, \tag{6}$$

where n is the polynomial degree, A_i is the Bernstein coefficient (or CST variables), and $\binom{n}{i}$ is the binomial coefficient.

Under the CST framework, the duct upper and lower surfaces are described as the product of the class and shape functions:

$$\begin{cases} \xi_{upper}(\psi) = \sqrt{\psi}(1-\psi) \cdot \sum_{i=0}^{n} A_{i,upper} \cdot \binom{n}{i} \psi^i (1-\psi)^{n-i} + \psi \Delta\xi_{upper}, \\ \xi_{lower}(\psi) = \sqrt{\psi}(1-\psi) \cdot \sum_{i=0}^{n} A_{i,lower} \cdot \binom{n}{i} \psi^i (1-\psi)^{n-i} + \psi \Delta\xi_{lower}. \end{cases} \tag{7}$$

Here, ψ and ξ are the foil–surface coordinates along the chord and thickness directions, respectively, normalized by the chord length, and $\Delta\xi$ specifies the trailing edge thickness, set at 0.5% of the chord length in this work. This CST parametrization offers systematic adjustments to

the upper and lower surfaces of the duct, ensuring smooth geometries throughout the design process.

Another advantage of using the CST variable is that the leading-edge radius of curvature can be directly expressed as

$$\tilde{\rho_\kappa} = \frac{1}{2}A_0^2, \tag{8}$$

for both upper and lower surfaces, where $\tilde{\rho_\kappa}$ is the radius of curvature normalized by the chord length. This is computed by first substituting the first and second derivatives of Eq. (7) into the general equation for radius of curvature, i.e., $\tilde{\rho_\kappa}(\psi) = \{1 + [\xi'(\psi)]^2\}^{3/2}/\xi''(\psi)$, and then taking the limit as $\psi \to 0$. For a detailed derivation, readers can refer to the appendix of the original paper [36].

Data availability

All data are included in the paper, with a link to the Git repository for key files provided: https://github.com/jbpark94/Ducted-Hydrokinetic-Turbine-Key-Files.git.

References

[1] A. Bahaj, L.E. Myers, Fundamentals applicable to the utilisation of marine current turbines for energy production, Renew. Energy 28 (2003) 2205–2211.

[2] W. Ibrahim, M. Mohamed, R. Ismail, P. Leung, W. Xing, A. Shah, Hydrokinetic energy harnessing technologies: A review, Energy Rep. 7 (2021).

[3] K. Kirby, S. Ferguson, C. Rennie, I. Nistor, J. Cousineau, Assessments of available riverine hydrokinetic energy: a review, Can. J. Civ. Eng. 49 (2022) 839–854.

[4] V.G. Nago, I.F.S. dos Santos, M.J. Gbedjinou, J.H.R. Mensah, G.L. Tiago Filho, R.G.R. Camacho, R.M. Barros, A literature review on wake dissipation length of hydrokinetic turbines as a guide for turbine array configuration, Ocean Eng. 259 (2022) 111863.

[5] M.I. Yuce, A. Muratoglu, Hydrokinetic energy conversion systems: A technology status review, Renew. Sustain. Energy Rev. 43 (2015) 72–82.

[6] L. Lago, F. Ponta, L. Chen, Advances and trends in hydrokinetic turbine systems, Energy Sustain. Dev. 14 (2010) 287–296.

[7] M.M. Nunes, A.C.B. Junior, T.F. Oliveira, Systematic review of diffuser-augmented horizontal-axis turbines, Renew. Sustain. Energy Rev. 133 (2020) 110075.

[8] C. Lawn, Optimization of the power output from ducted turbines, Proc. Inst. Mech. Eng. Part A: J. Power Energy 217 (2003) 107–117.

[9] G.J. Van Bussel, The science of making more torque from wind: Diffuser experiments and theory revisited, in: Journal of Physics: Conference Series, Vol. 75, IOP Publishing, 2007, 012010, http://dx.doi.org/10.1088/1742-6596/75/1/012010.

[10] M.J. Werle, W.M. Presz Jr., Ducted wind/water turbines and propellers revisited, J. Propuls. Power 24 (2008) 1146–1150.

[11] R. Bontempo, M. Manna, On the potential of the ideal diffuser augmented wind turbine: an investigation by means of a momentum theory approach and of a free-wake ring-vortex actuator disk model, Energy Convers. Manage. 213 (2020) 112794, http://dx.doi.org/10.1016/j.enconman.2020.112794.

[12] F. Scherillo, U. Maisto, G. Troise, D. Coiro, S. Miranda, Numerical and experimental analysis of a shrouded hydroturbine, in: 2011 International Conference on Clean Electrical Power, ICCEP, IEEE, 2011, pp. 216–222.

[13] M. Shahsavarifard, E.L. Bibeau, V. Chatoorgoon, Effect of shroud on the performance of horizontal axis hydrokinetic turbines, Ocean Eng. 96 (2015) 215–225.

[14] M.M. Nunes, R.C. Mendes, T.F. Oliveira, A.C.B. Junior, An experimental study on the diffuser-enhanced propeller hydrokinetic turbines, Renew. Energy 133 (2019) 840–848.

[15] C.F. Fleming, R.H. Willden, Analysis of bi-directional ducted tidal turbine performance, Int. J. Mar. Energy 16 (2016) 162–173.

[16] M. Shives, C. Crawford, Developing an empirical model for ducted tidal turbine performance using numerical simulation results, Proc. Inst. Mech. Eng. Part A: J. Power Energy 226 (2012) 112–125.

[17] W. Shi, D. Wang, M. Atlar, B. Guo, K. c. Seo, Optimal design of a thin-wall diffuser for performance improvement of a tidal energy system for an auv, Ocean Eng. 108 (2015) 1–9.

[18] S. Allsop, C. Peyrard, P.R. Thies, E. Boulougouris, G.P. Harrison, Hydrodynamic analysis of a ducted, open centre tidal stream turbine using blade element momentum theory, Ocean Eng. 141 (2017) 531–542.

[19] K. Song, W.-Q. Wang, Y. Yan, Numerical and experimental analysis of a diffuser-augmented micro-hydro turbine, Ocean Eng. 171 (2019) 590–602.

[20] B. Knight, R. Freda, Y.L. Young, K. Maki, Coupling numerical methods and analytical models for ducted turbines to evaluate designs, J. Mar. Sci. Eng. 6 (2018) 43.

[21] M. Barbarić, Z. Guzović, Investigation of the possibilities to improve hydrodynamic performances of micro-hydrokinetic turbines, Energies 13 (2020) 4560.

[22] T. Rezek, R. Camacho, N. Manzanares Filho, E. Limacher, Design of a hydrokinetic turbine diffuser based on optimization and computational fluid dynamics, Appl. Ocean Res. 107 (2021) 102484.

[23] J.R.R.A. Martins, A. Ning, Engineering Design Optimization, Cambridge University Press, Cambridge, UK, 2022, http://dx.doi.org/10.1017/9781108980647, URL: https://mdobook.github.io.

[24] J. Park, B.G. Knight, Y. Liao, M. Mangano, B. Pacini, K.J. Maki, J.R. Martins, J. Sun, Y. Pan, CFD-based design optimization of ducted hydrokinetic turbines, Sci. Rep. 13 (2023) 17968.

[25] A. Bahaj, A. Molland, J. Chaplin, W. Batten, Power and thrust measurements of marine current turbines under various hydrodynamic flow conditions in a cavitation tunnel and a towing tank, Renew. Energy 32 (2007) 407–426.

[26] R. Haimes, J. Dannenhoffer, The Engineering Sketch Pad: A solid-modeling, feature-based, web-enabled system for building parametric geometry, in: 21st AIAA Computational Fluid Dynamics Conference, Fluid Dynamics and Co-Located Conferences, American Institute of Aeronautics and Astronautics, 2013, http://dx.doi.org/10.2514/6.2013-3073.

[27] H.M. Hajdik, B. Pacini, A. Yildirim, B.J. Brelje, J.R.R.A. Martins, Combined systems packaging and aerodynamic shape optimization of a full aircraft configuration, in: AIAA Aviation Forum, San Diego, CA, 2023, http://dx.doi.org/10.2514/6.2023-3589.

[28] G.K. Kenway, G.J. Kennedy, J.R.R.A. Martins, A CAD-free approach to high-fidelity aerostructural optimization, in: Proceedings of the 13th AIAA/ISSMO Multidisciplinary Analysis Optimization Conference, AIAA 2010-9231, Fort Worth, TX, 2010, http://dx.doi.org/10.2514/6.2010-9231.

[29] J. Dannenhoffer, An overview of the engineering sketch pad, in: AIAA SCITECH 2024 Forum, 2024, p. 1315.

[30] M. Mangano, J.R.R.A. Martins, Multipoint aerodynamic shape optimization for subsonic and supersonic regimes, J. Aircr. 58 (2021) 650–662, http://dx.doi.org/10.2514/1.C036216.

[31] P. He, C.A. Mader, J.R.R.A. Martins, K.J. Maki, DAFoam: An open-source adjoint framework for multidisciplinary design optimization with OpenFOAM, AIAA J. 58 (2020) http://dx.doi.org/10.2514/1.J058853.

[32] P.E. Gill, W. Murray, M.A. Saunders, SNOPT: An SQP algorithm for large-scale constrained optimization, SIAM Rev. 47 (2005) 99–131, http://dx.doi.org/10.1137/S0036144504446096.

[33] H. Jasak, A. Jemcov, Z. Tukovic, et al., OpenFOAM: A C++ library for complex physics simulations, in: International Workshop on Coupled Methods in Numerical Dynamics, Vol. 1000, Dubrovnik, Croatia, 2007, pp. 1–20.

[34] USGS water data for Mississippi River at Baton Rouge, LA, 2024, https://waterdata.usgs.gov/monitoring-location/07374000/. (Accessed 28 October 2024).

[35] M. Tariquzzaman, P. Li, S.J. Barton, A.P. Thurlbeck, T. Kilgore, T.K. Brekken, Y. Cao, Multi-physics and multi-timescale modeling of hydrokinetic turbine energy conversion system, IEEE J. Emerg. Sel. Top. Power Electron. (2024).

[36] B. Kulfan, J. Bussoletti, Fundamental parametric geometry representations for aircraft component shapes, in: 11th AIAA/ISSMO Multidisciplinary Analysis and Optimization Conference, 2006, p. 6948.

[37] R. Venters, B.T. Helenbrook, K.D. Visser, Ducted wind turbine optimization, J. Sol. Energy Eng. 140 (2018) 011005.

[38] P. Spalart, S. Allmaras, A one-equation turbulence model for aerodynamic flows, in: 30th Aerospace Sciences Meeting and Exhibit, 1992, http://dx.doi.org/10.2514/6.1992-439.

[39] E. Luke, E. Collins, E. Blades, A fast mesh deformation method using explicit interpolation, J. Comput. Phys. 231 (2012) 586–601, http://dx.doi.org/10.1016/j.jcp.2011.09.021.

[40] N. Secco, G.K.W. Kenway, P. He, C.A. Mader, J.R.R.A. Martins, Efficient mesh generation and deformation for aerodynamic shape optimization, AIAA J. 59 (2021) 1151–1168, http://dx.doi.org/10.2514/1.J059491.

[41] F.R. Menter, M. Kuntz, R. Langtry, et al., Ten years of industrial experience with the SST turbulence model, Turbul. Heat Mass Transf. 4 (2003) 625–632.

[42] M. Badshah, J. VanZwieten, S. Badshah, S. Jan, Cfd study of blockage ratio and boundary proximity effects on the performance of a tidal turbine, IET Renew. Power Gener. 13 (2019) 744–749.

[43] K. Song, H. Huan, Y. Kang, Aerodynamic performance and wake characteristics analysis of archimedes spiral wind turbine rotors with different blade angle, Energies 16 (2022) 385.

[44] B. Brelje, Multidisciplinary Design Optimization of Electric Aircraft Considering Systems Modeling and Packaging (Ph.D. thesis), University of Michigan, Ann Arbor, MI, 2021, http://dx.doi.org/10.7302/2703.

[45] G. Kalitzin, G. Medic, G. Iaccarino, P. Durbin, Near-wall behavior of rans turbulence models and implications for wall functions, J. Comput. Phys. 204 (2005) 265–291.

[46] J.C. Hunt, A.A. Wray, P. Moin, Eddies, streams, and convergence zones in turbulent flows, studying turbulence using numerical simulation databases, in: Proceedings of the 1988 Summer Program 1988, Vol. 2.

[47] M.A. Rahmatian, P.H. Tari, M. Mojaddam, S. Majidi, Numerical and experimental study of the ducted diffuser effect on improving the aerodynamic performance of a micro horizontal axis wind turbine, Energy 245 (2022) 123267.